Sánchez-Arriaga, G.; Borderes-Motta, G.; Chiabó, L. A code for the analysis of missions with electrodynamic tethers. In: *Acta astronautica, vol. 198, Sept. 2022, Pp. 471-481*

DOI: https://doi.org/10.1016/j.actaastro.2022.06.021

A Code for the Analysis of Missions with Electrodynamic Tethers

Gonzalo Sánchez-Arriaga[1], Gabriel Borderes-Motta[2], Luca Chiabó[3]

Department of Bioengineering and Aerospace, Universidad Carlos III de Madrid - Madrid (Spain)

Abstract

The main novelties and capabilities of the second version of the Bare Electrodynamic Tether Mission Analysis Software (BETsMA v2.0) are presented. Recent advances on Orbital-Motion-Theory have been incorporated to the electric model of Low-Work-function Tethers (LWTs). An electric model that considers a switch to embed a power supply or a resistor between a Bare Electrodynamic Tether (BET) and an electron emitter is also introduced. For both types of tethers (LWT and BET) and modes of operations (active and passive), robust and efficient numerical algorithms to compute the current and voltage profiles were constructed based on a change of variable proposed in a previous work. The capabilities of the code are illustrated by considering two relevant scenarios. For a BET in the passive mode, it was shown that onboard power can enhance tether performance and reduce significantly the deorbit time. For a BET in the active mode, a performance map varying the orbit inclination, the length of the insulated tether segment, and the power was constructed. For both cases, the code was used to investigate through simulations the conditions to keep constant the electric current at the electron emitter.

Keywords: Electrodynamic Tether, Space Debris, Electric Propulsion.

---

[1] gonzalo.sanchez@uc3m.es
[2] gabriel.borderes@uc3m.es
[3] lchiabo@pa.uc3m.es

Preprint submitted to Acta Astronautica *June 13, 2022*

1. Introduction

The ongoing transformation of the space sector, including new companies, investors, and the launch of mega-constellations, poses new challenges for policymakers due to the proliferation of space debris [1]. It is also expected to trigger in the next future new business opportunities related to on-orbit servicing, post-mission disposal, and the use of orbits at very low altitudes. Some of these applications can benefit from the use of Electrodynamic Tethers (EDTs) that, unlike conventional propulsion technologies, exchange momentum with the planet's magnetosphere with no need for propellant (find a review in [2]). In particular, a Bare EDT (BET) equipped with an Active electron Emitter (AEE) operating in the so-called *passive* mode in Low Earth Orbit (LEO) produces a drag that deorbits the S/C while providing power for onboard use. If onboard power is available, a BET in the *active* mode produces a thrust that can be used to compensate the air drag or reboost the S/C [3].

Recently, considerable progress has been made to push the development of EDT technology forward. Relevant examples include the transition from round to tape tethers [4, 5, 6], the appearance of new consumable-less solutions to achieve a good cathodic contact with the ambient plasma such as the Low-Work-Function Tether (LWT) concept [7, 8] and new and improved active electron emitters [9], and novel ideas to enhance EDT's performance and simplicity such as the bare-photovoltaic tether [10]. Advances in materials science [11] and the miniaturisation of space components [12] are also important. Combined with their versatility, such developments resulted in a renewed interest in EDTs. TEPCE by the U.S. Naval Research Laboratory, Dragracer by Millennium Space Systems with a tape tether made by Tether Unlimited, DESCENT [13], and MiTEE [12] are some examples of recent missions with tethers. In Europe, the E.T.PACK consortium is preparing an EDT-based deorbit device [14].

Simulation tools play a key role on EDT development at two different levels. Firstly, they provide support for carrying out the mission design, including the detumbling and the tether deployment preparation phases, and the nominal operation. The results of such analyses help for instance to select appropriate sensors and actuators of the Attitude and Orbit Control System [15]. Secondly, accurate and flexible simulation tools are necessary to assess EDT's performance and allow non-experts and potential investors to evaluate the technology, explore the use of EDTs in new scenarios, and make decisions. Accordingly, research groups and companies have developed EDT simulators with different degree of accuracy, complexity and computational cost like TEMPEST [16], FLEX [17], DYNATETHER [18], TetherSim^{TM} [19], and BETsMA [20] among many others [21, 22, 23, 24, 25, 26, 27, 28]. A central element of these software is the electric module, i.e. the numerical algorithm in charge of computing the current and voltage profiles throughout the tether. Being necessary at every time step to evaluate the Lorentz force and torque, these algorithms received an important attention in past works [29, 30, 31, 18] and severely affect the computational cost, robustness, and fidelity of the simulators.

This work presents a comprehensive description of the second version of the Bare Electrodynamic Tether Mission Analysis Software (BETsMA v2.0). Section 2 explains the EDTs types and modes and sub-modes of operation implemented in the software. A detailed description of the electric module is given in the Appendixes. Among its main novelties, we highlight here the incorporation of new results in probe theory to tether modelling, the extension of a previously proposed parametrization strategy to improve the efficiency of the numerical algorithms, and the incorporation of a power supply to enhance the performances of EDTs in the passive mode. The combination of a power source with a tether was studied in several previous works [3, 19, 32], but mainly restricted to the so-called active mode for boosting in LEO. This work presents an electric model that combines a power source with a bare tether in passive mode to enhance deorbiting performances. This is relevant for EDT systems like EDDE [32], which are equipped with solar arrays, and in post-mission disposal scenarios if the solar panels of the satellite are still operative. Simulation results in the passive and the active modes are presented in Sec. 3. Finally, Sec. 4 summarizes the conclusions. Complementary to this work, an online interface to submit simulations using BETsMA v2.0 has been published [33].

2. The BETsMA v2.0 software

2.1. Basic Information

The first version of the BETsMA software was developed in the framework of the FP7/Space project with acronym BETs (2010-2014). Focused on the simulation of missions by using bare tethers in the passive mode, the software also implemented the $\Pi - algorithm$ for the optimal sizing of tethers [34]. Detailed information about BETsMA v1.0 is available in a manual [35] and a scientific work [20]. As part of the activities of the FET project with acronym E.T.PACK (2019-2022) [14], a second version has been prepared. Table 1 summarizes its capabilities and provides appropriate references to the scientific works that explain in detail the physical models and mathematical algorithms. Regarding tether dynamics, tether attitude can be constrained (tether aligned with the local vertical or spinning at a prescribed angular velocity), or be found self-consistently with a dynamic model that substitutes the tether by a set of N inelastic and articulated bars or a set of particles linked by springs and dampers. Since this work is focused on the electric models and the preliminary mission design, all the simulations in this study assumed a straight tether aligned with the local vertical. Other upgrades are the tether thermal model presented in [2], the incorporation of high harmonics of the Earth's gravitational field, and some improvements related to the numerical methods, like adding a numerical integrator with a variable time step and two types of stop conditions in the simulations. The upgrades of BETsMA v2.0 are highlighted with bold font in table 1.

BETsMA v2.0 computes the cut probability by small debris of round and tape-like tethers using the model in Ref. 4 and considering the debris flux of ORDEM-2000 or MASTER-2009. All the results of this work have been found with MASTER-2009 that, as explained below, may be an adequate choice for conservative estimations. For circular orbits with altitude below 800 kilometers and two different inclinations (60° and 98°), we compared the space debris flux for the small debris size (below 1 meter) given by MASTER-2009 and the latest version MASTER 8, which considers 2016 as reference year. Depending on the altitude, the inclination and the debris size, we found that the flux provided by MASTER 8 is a factor between 2 and 8 lower. This is because the minimum and the maximum of the solar cycle 24 happened in 2008 and 2014, respectively. The former are periods where the small space debris accumulates and the latter, i.e. the solar maximum, have a cleansing effect. The Fengyun-1C anti-satellite test in 2007 and Cosmos-Iridium in 2009, that resulted in a high number of small debris, were close to the reference year of MASTER-2009. Many of these fragments were removed during the solar maximum of 2014, which preceded the reference year of Master 8. This data suggests that MASTER-2009 is adequate for the preliminary analysis of missions using EDTs. However, it is desirable that future versions of BETsMA v2.0 will contain updated values of the debris flux for, at least, two years (corresponding to solar minimum and maximum).

Although it does not affect to tether performances in the actual version of the software, BETsMA v2.0 provides an estimation of the total number of ATOX impacting the tether during the mission. Such information is important due to the negative effect of ATOX on certain materials. For a tether of perimeter p_t and length L_t, the aerodynamic drag is computed by using a cross-sectional area of $p_t L_t/\pi$, which is valid for round and tape-like tethers. All the environmental models depend on time, except the ones related with the debris flux that are found from ORDEM-2000 or MASTER-2009 models. Besides limitations arising from the physical assumptions used to construct the models, which should be known by the user as part of the common know-how on tethers, there are no limitation for any of the physical parameters. The only exception is the maximum duration of the simulations because the mission should finish by the end of 2015 due to limitations related with the actual implementation of the environmental model. However, this is minor issue because an appropriate starting date can be found by taking into account past and actual data of the solar cycle.

BETsMA v2 includes electric models for BETs [3] and LWTs [7, 8, 40] in both passive and active modes. The operation mode depends on the directions

Table 1: Characteristics and physical and mathematical models of BETsMA v2. SCL and RD refers to passive electron emission by the tether in Space-Charge-Limited conditions and following Richardson Dushman law, respectively. Upgrades with respect to the first version of the software are highlighted in bold.

Environmental Models	
Gravitational field	**Up to 4th order harmonics**
Magnetic field	Dipole/Eccentric Dipole/IGRF [36]
Ionospheric Plasma	IRI [37]
Air density	CIRA [38]/**NRLMSISE-00** [39]
ATOX	**NRLMSISE-00** [39]
Debris flux	MASTER-2009/ORDEM-2000
Tether Models	
Tether Type	BET [3]/**LWT** [7, 8, 40]
Tether Cross-section	Round/Tape
Tether Attitude	Aligned with local vertical/spinning/ **N-bar model** [41] **N-particle model** [41]
Thermal Model	**Local balance** [2]
Operation mode	Passive/**Active**
Electron collection laws	OML [3]/Beyond OML [42, 31]
Electron emission laws	EE with potential drop V_C, **SCL + RD** [43]
Perturbation forces	Lorentz force Aerodynamic drag. **Gravitational potential harmonics**
Algorithms	
Orbit propagator	DROMO [44]
Tether sizing tool	π-algorithm [34]
Numerical integrator	Runge–Kutta–Fehlberg (RKF45) **RADAU**
Stop conditions	Final altitude/ **Mission duration**

of the tether current ($\boldsymbol{I} = I(x)\boldsymbol{u}_t$) and the motional electric field in the tether frame ($\boldsymbol{E}_m = \boldsymbol{v}_{rel} \times \boldsymbol{B}$) that appears in the unperturbed plasma due to the tether-to plasma relative velocity ($\boldsymbol{v}_{rel}$) and the ambient magnetic field ($\boldsymbol{B}$) [3]. Here, x is the coordinate along the straight tether measured from the anodic point A and $\boldsymbol{u}_t$ is an unit vector along the tether and pointing from the cathodic point (C) to the anodic point (A) as shown in Figs. 1 and 2. In the passive mode, one has $\boldsymbol{E}_m \cdot \boldsymbol{I} > 0$ and, in LEO, the Lorentz force

$$\boldsymbol{F}_L = \int_0^{L_a} \boldsymbol{I} \times \boldsymbol{B} dx \approx L_a I_{av} \left(\boldsymbol{u}_t \times \boldsymbol{B} \right) \tag{1}$$

is a drag ($\boldsymbol{F}_L \cdot \boldsymbol{v} < 0$) that deorbits the S/C. Symbols L_a, $\boldsymbol{v}$, I_{av} denote the length of the tether segment that carries the electric current, the velocity of the S/C, and the average current along the tether.

$$I_{av} = \frac{1}{L_a} \int_0^{L_a} I(x) dx \tag{2}$$

In the active mode, a power supply is needed to make $\boldsymbol{E}_m \cdot \boldsymbol{I} < 0$ and, in LEO, the Lorentz force is a thrust ($\boldsymbol{F}_L \cdot \boldsymbol{v} > 0$) that can be used to re-boost the S/C or compensate the aerodynamic drag. The average current in Eq. (1) is found by integrating the current profile $I(x)$ along the EDT. Therefore, I_{av} depends on the type of EDT, its longitudinal structure, and the operation mode.

2.2. Description of the EDT Systems

Figure 1 shows the longitudinal structure of the two EDTs considered by BETsMA v2 in the passive mode. Both of them have an inert (non-conductive) segment between points Z and A of length L_{inert}. This segment does not contribute to the Lorentz force in Eq. (1), but increases the aerodynamic drag and is convenient to enhance the gravity gradient restoring torque and mitigate the dynamic instability of EDTs [21].

In the case of the BET (top panel in Fig. 1), the software considers a bare segment of length L_b between points A and P, and a conductive and insulated segment of length L_i between point P and the S/C (points S_i). The former is in charge of the passive electron collection and the latter is used to avoid an electric

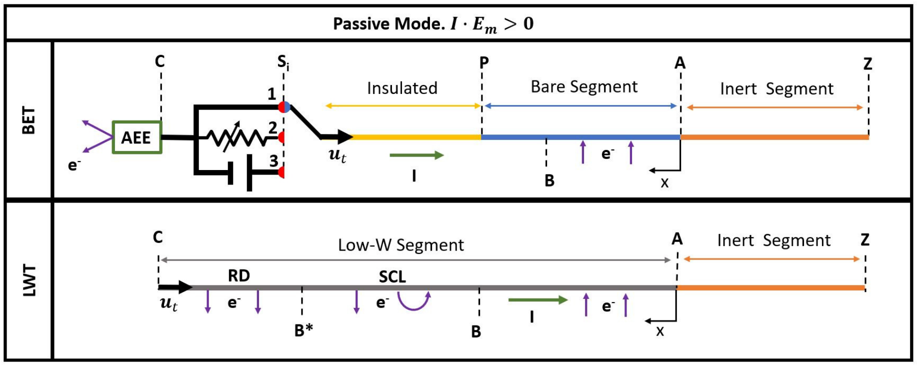

Figure 1: Longitudinal structures of a BET (top) and a LWT (bottom) in passive mode.

arc between the tether and the S/C. The total length of the active segment in Eq. (1) is $L_a = L_b + L_i$. At the S/C, the model considers a switch with three possible connections that can be changed during the mission. The electric current can flow through different electric elements between points S_i, with $i = 1, 2, 3$, and the AEE, which emits any current at the cost of a potential drop $V_C < 0$. When connected through path S_1, S_2, and S_3, the insulated segment is connected directly to the AEE, a variable resistor with resistance $R(t)$, or a power supply that delivers an electric power W_e, respectively. The switch provides 5 sub-modes of operation for the BET in passive mode: [i] standard ($R = W_e = 0$), [ii] power harvesting ($R = R_0$ and $W_e = 0$), [iii] current limited ($W_e(t)$ and $R(t)$ determined dynamically to make the current at the cathode (I_C) be below certain maximum I_C^{max}), [iv] constant power ($R = 0$ and $W_e = W_{e0}$), and (v) constant current [$R(t)$ and $W_e(t)$ are adjusted dynamically to make $I_C = I_C^*$]. As shown in Table 2, the state of the switch is fixed for each sub-mode, except for the current limited and the constant current sub-modes, where the switch state is dynamically changed during the simulation between points S_1 and S_2 and S_2 and S_3, respectively. The particular operation sub-mode and constants R_0, W_{e0} and I_C^* are part of the configuration of the simulation. Additionally, it is possible to add constraints on the maximum available power and allowed current at the cathode [find more details in Sec. 3 that presents simulations for the sub-modes (i), (iv), and (v)].

Table 2: Summary of the sub-modes implemented in BETsMA v2.0 .

Mode	Sub-mode	Switch State	Characteristics
Passive	Standard	S_1	$R(t) = W_e(t) = 0$
	Power Harvesting	S_2	$R(t) = R_0,\ W_e(t) = 0$
	Current Limited	S_1, S_2	$R(t)$ and $\mathrm{W_e(t)\backslash I_C(t) \leq I_C^{max}}$
	Constant Power	S_3	$R(t) = 0,\ W_e(t) = W_{e0}$
	Constant Current	S_2, S_3	$R(t)$ and $\mathrm{W_e(t)\backslash I_C(t) = I_C^{*}}$
	Standard	N/A	$W_e(t) = W_{e0}$
	Constant Current	N/A	$W_e(t)\backslash I_C(t) = I_C^{*}$
	Station-keeping	N/A	$W_e(t)\backslash\,(\boldsymbol{F_L} + \boldsymbol{F_A}) \cdot \boldsymbol{v} = 0$

For the LWT (bottom panel in Fig. 1), the full active tether is coated with a Low-W material. The tether itself is responsible for the passive electron collection between point A and the (zero-bias) point B and the passive electron emission between points B and B^* in space-charge-limited (SCL) conditions and between B^* and C according to the Richardson-Dushman (RD) law. Since coated with a Low-W material, segment $A - B^*$ also emits electrons. However, these electrons are captured again by the LWT because it is positively polarized with respect to the plasma in that segment. Similar to the top panel, it would be possible to prepare configurations combining a LWT with a resistor to harvest electric power or with a power supply to improve the performance. Currently, these sub-modes of operation are not implemented in BETsMA v2 for LWTs.

As shown in Fig. 2, the longitudinal structure of both tether types in active mode are very similar. Moving from point Z to S, one finds an inert (non-conductive segment), a bare segment for electron collections, a conductive and insulated segment to avoid electric arcing and improve the efficiency [3], and the positive pole of a power supply that provides an electric power W_e. For BETs (LWTs), the negative pole of the power supply is connected to an AEE (a tether segment of length L_c and coated with a low-W material). Three sub-modes of operation have been implemented for EDTs in active mode (see Table 2): [i] constant power ($W_e = W_{e0}$), [ii] constant current (the power is adjusted dynamically to reach $I_C = I_C^*$), and [iii] station-keeping (the power is dynamically adjusted to meet the condition $(\boldsymbol{F}_L + \boldsymbol{F}_A) \cdot \boldsymbol{v} = 0$ with $\boldsymbol{F}_A$ the total aerodynamic force on the tether and the S/C).

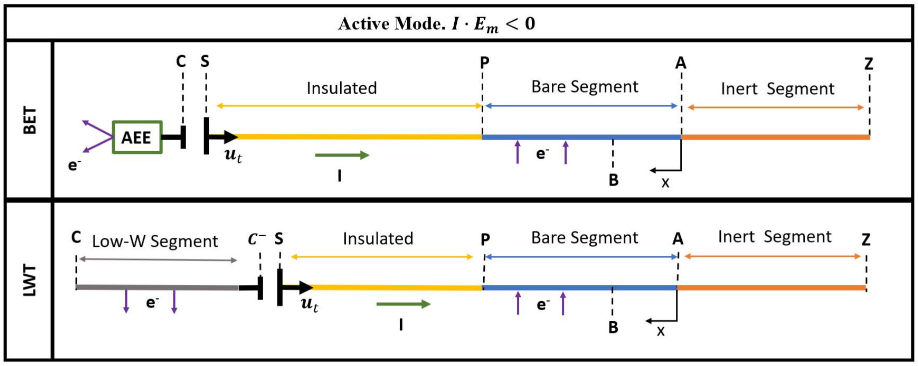

Figure 2: Longitudinal structures of a BET+AEE (top) and a LWT (bottom) in active mode.

2.3. Electric Module

As shown in previous works on BETs [3, 45, 46] and LWTs [7][43][8][40], computing the current profile $I(x)$ for each of the four configurations in Fig. 1 and 2 requires a specific analysis. For convenience, we moved the mathematical details to the Appendix and enumerate here the main novelties and contributions of this work. Firstly, a recent progress on Orbital-Motion-Theory to determine the SCL/non-SCL transition point [47] was incorporated in the LWT model, thus improving the accuracy of the physical model. Secondly, the parametrization strategy first proposed in Ref. [31] for BETs in the passive mode has been extended to cover BETs in the active mode and LWTs in the passive and the active modes. As shown in Sec. 3, it impacted notably on the efficiency and robustness of the software. We finally highlight the complex longitudinal structures of the tethers shown in Figs. 1 and 2, and the use of a power supply in the passive mode.

For convenience, we now analyze the impact of the input power on the average current I_{av} of a BET in the passive mode. Since this is a novel feature of the electric model, an analysis is needed before presenting simulation results in Sec. 3. As shown in Appendix B, the normalized average current i_{av} of a BET with cross-sectional area A_t and conductivity σ_t depends on the normalized potential drop of the AEE (ϕ_C), the dimensionless resistance (r) and input power (w_e), and the normalized lengths of the insulated (ξ_i) and bare (ξ_b) tether segments [find the definitions of these parameters in Eqs. (A.16) and (A.17)]

$$\frac{I_{av}}{\mid E_m \mid \sigma_t A_t} \equiv i_{av}\left(\xi_b, \xi_i, \phi_C, r, w_e\right) \tag{3}$$

For a conventional BET (i.e., $\xi_i = \phi_C = r = w_e = 0$), one has $i_{av} \leq 1$ for all ξ_b. In particular, i_{av} admits the approximate form $i_{av} \approx 0.3\xi_b^{3/2}$ for $\xi_b << 1$ and the exact form $i_{av} = 1 - 1/\xi_b$ for $\xi_b \geq 4$ [45, 48]. A natural question is the effect of w_e on i_{av}.

The thick solid lines in panels (a)-(c) in Fig. 3 show i_{av} versus ξ_b for $\xi_i = \phi_C = r = w_e = 0$. The other lines correspond to the same parameters, except the ones indicated in the labels. For instance, panels (a) and (b) display the effect of the potential drop of the AEE and the electrical resistance of the resistor, respectively. They provide evidence about the correct implementation of the electric model because they coincide with previous results in the literature [45, 31]. Panel (c) shows the impact of adding a power supply that works collaboratively with the motional electric field. Clearly, tether performances are improved and, similarly to bare-photovoltaic tethers [10], the average current can exceed the short-circuit current ($i_{av} > 1$) for a high enough input power.

It is well-known that, as compared with a fully bare EDT, insulating a tether segment close to the power supply of an EDT in active mode improves its efficiency [3, 40]. This statement holds because the electrons collected close to the power supply contribute little to the force but consume energy from the power supply. In general, the same result applies for an EDT in passive mode and equipped with a power supply. However, the impact of the insulated segment is modest because the bias is the largest near the power supply for a

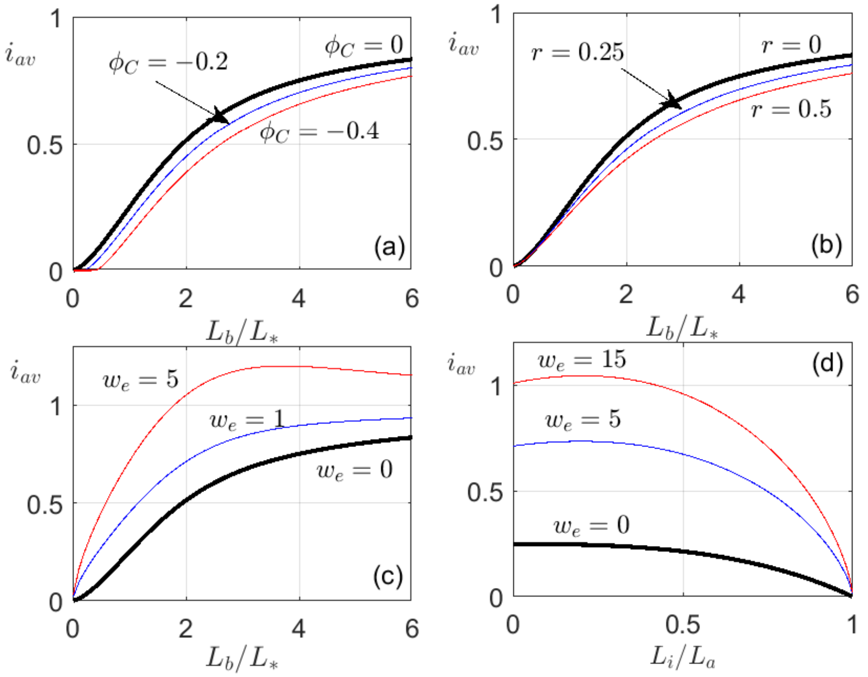

Figure 3: Panels (a)-(c) show i_{av} versus $\xi_b \equiv L_b/L_*$ for $\xi_i = r = \phi_C = w_e = 0$ (except otherwise indicated). Panel (d) displays i_{av} versus L_i/L_a for $L_a/L_* = 1$, $r = \phi_C = 0$, and several values of w_e.

tether in active mode but the lowest for the proposed tether in the passive mode. In fact, it is negative (and there is no electron collection) for real AEE ($\phi_C < 0$). These comments are corroborated by panel (d) in Fig. 3, which shows i_{av} versus the ratio L_i/L_a for $r = \phi_C = 0$, $L_a = L_b + L_i = L_*$, and several input powers. For $w_e = 0$, insulating a tether segment always deteriorates the performance in the passive mode. The larger the insulated fraction, the lower i_{av}. However, for $w_e \neq 0$, i_{av} exhibits a maximum at a certain fraction of L_i/L_a. Nonetheless, as advanced, the improvement in the performances is modest. For this reason, we will take $L_i = 0$ in our simulations in the passive mode.

3. Simulation results

This section presents simulations with BETsMA v2.0 in deorbiting and reboost scenarios. Emphasis is made on the deorbiting maneuver aided by onboard power, and in deorbiting/reboost missions with constant current by varying dynamically the resistance of the resistor and the supplied power. Due to their larger maturity as compared to LWTs, we focus the analysis on BETs.

IRI, IGRF, NRLMSISE-00, MASTER-2009, and up to 4th order harmonics are used for computing the plasma density, the magnetic field, the density of neutrals, the flux of small debris, and the Earth's gravitational field. The tether is always aligned with the local vertical. Table 3 summarizes the parameters used in the simulations. We consider a 500-kg satellite with ballistic coefficient $\beta_S = 50\ kg/m^2$ orbiting initially in a circular orbit. The drag coefficients of the satellite and the tether are $C_D = 2$. The tether has a total length of 2 km and a tape-like cross-section of dimensions 2.5 $cm \times 40\ \mu m$. The potential drop of the AEE is $V_C = -30\ V$. The starting date of the simulated missions is January 1st, 2000.

Table 3: Parameters of the simulation.

Property	Value	Property	Value
H_0	800 km	H_F	300 km
L_a	2000 m	L_{inert}	0
w_t	2.5 cm	h_t	40 μm
σ_t	$3.54 \times 10^7\ 1/\Omega m$	ρ_t	2700 kg/m^3
M_S	500 kg	V_C	-30 V
C_D	2	β_S	50 kg/m^2

3.1. EDT in passive mode

3.1.1. The constant power submode

We first study the deorbiting from an orbit of 800 km of altitude. The mission is considered accomplished when the altitude reaches 300 km. Following the conclusions of Sec. 2.3, we set $L_i = 0$ and then $L_a = L_b = 2$ km. The input power is constant in the simulations, except when the electric current at the AEE exceeds $I_{max} = 5\ A$. For these particular time steps, the electric module first finds the required power to have $I_C = I_{max}$ at the AEE and then compute the current and voltage profiles accordingly.

Panels (a) and (b) in Fig. 4 show the deorbit time obtained in a set of simulations varying the inclination of the initial orbit. For clarity, different limits in the vertical axes were used in these two panels. For inclination below 60°, the EDT deorbits the satellite in less than 2 months without any power and the tether cut probability by small debris is well below 1% [panels (c) and (d)]. For higher inclinations, EDT's performances obviously decrease and the benefits of using available onboard power to improve tether performances become evident. For instance, for the interesting commercial case of Sun-Synchronous orbits (98° of inclination), the deorbit time for $W_e = 0$, 50, 100, 250 and 500 W are 277, 183, 158, 128 and 108 days and the cut probabilities are 1.25, 0.78, 0.68, 0.54 and 0.45%. As compared with the case with $W_e = 500$ W, increasing the power to 1 kW (not shown) does not improve considerably the performances. These results show that even relatively short EDTs (2 km) can be used for the fast deorbiting (within a few months) of heavy satellites (500 kg) from high-inclined orbits if the available onboard power is used.

For simulations with constant power, the electric current can reach high instantaneous values. For instance, the dashed black line in panel (a) of Fig. 5 shows that the evolution of the current at the cathode for a simulation with $i = 60°$ and $W_e = 100$ W takes values above several amps. Since the tether conductivity is assumed to be constant, and the AEE can emit any current at the cost of a potential drop that is constant in the actual version of the software, these high currents raise the question about the impact of these hypotheses on the results. To get some insight, we ran a set of simulations varying the inclination and using BETsMA v2.0 in the current limited mode with 100 W of available power. The input power (or the value of the resistor) were adjusted dynamically in the simulation to have a current at the cathode below 1.5 A. It

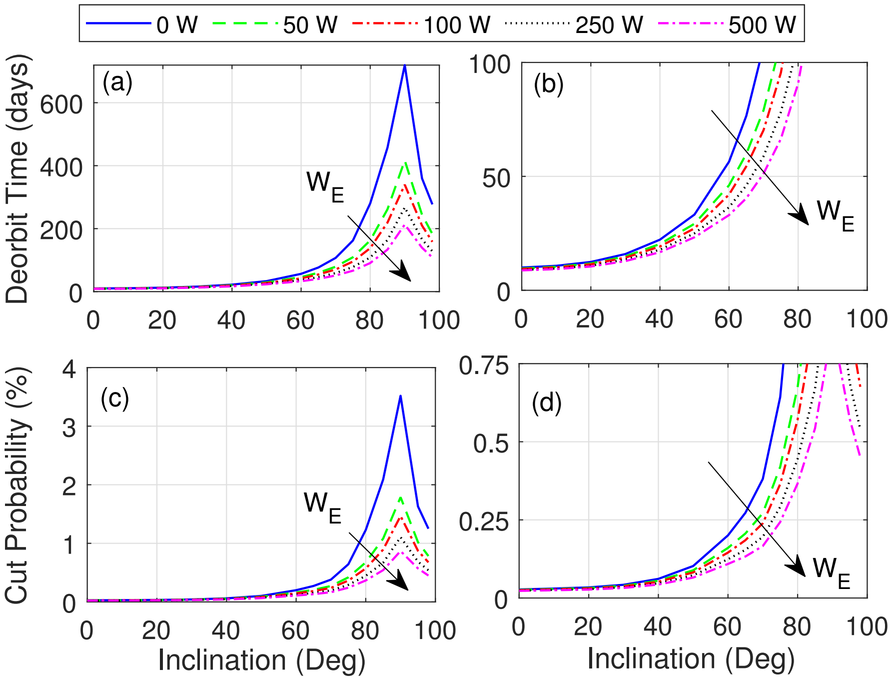

Figure 4: Simulation results of the deorbit time versus initial orbit inclination for the parameters in Table 3.

was found that the impact on the performances is moderate. For instance, in the worst case of $i = 90^\circ$, the deorbit time increased less that 10%.

The impact of the solar cycle on the tether performances was investigated by repeating the simulations for $W_e = 100$ W in Fig. 4, but now using 1/1/1995 as the starting date. This date corresponds to a solar minimum and, since the plasma and air densities are lower, the electrodynamic and the aerodynamic drag decrease and the deorbit time increases. For inclinations up to 65°, we found that the deorbit time is a factor two higher than the one presented in Fig. 4. Such a factor grows linearly up to a maximum of 2.8 for 90° of inclination and drops to 2.4 at Sun-synchronous orbit. Since the initial altitude is high (800 km), the Lorentz drag is clearly dominant over the aerodynamic drag for most of the simulation.

3.1.2. The constant current submode

Keeping constant the current at the cathode can help to avoid the instabilities that can appear in certain AEE like hollow cathodes for low current levels and also to maximize their lifetime. The scenario is illustrated by considering the parameters of Sec. 3.1.1 and an initial inclination of 60°. Given a target current I_C^* and a maximum available power W_e^{max}, the software determines at every time step the resistance R of the resistor and the input power W_e of the power supply that satisfy the condition $I_C(t) = I_C^*$ under the constraint $W_e(t) < W_e^{max}$. It starts by computing I_{C0}, which is the current at the cathode for $R = W_e = 0$. If $I_{C0} > I_C^*$, then the code finds the value of R to have $I_C = I_C^*$. If $I_{C0} < I_C^*$, it computes I_C^{max}, which is the current at the cathode for the maximum available power W_e^{max}. For $I_C^{max} < I_C^*$, the code sets the power equal to W_e^{max}. Otherwise, it determines W_e in order to meet the condition $I_C = I_C^*$. Once the input power and the resistance are known, the code computes the current and voltage profiles needed for the Lorentz force.

Solid red lines in panels (a), (c), and (e) of Fig. 5 show the current at the cathode, the power provided by the power supply, and the power dissipated in the resistor for $I_C^* = 1$ Amp and $W_e^{max} = 100$ W. The right panels present a detail of the same magnitudes around the tenth day of the mission. For convenience, the results of the simulation in the *standard* mode ($W_e = R = 0$, dashed black lines) are also included. As shown in panel (a), the electric current has very large variations in the standard mode: from zero (when $\boldsymbol{E}_m \cdot \boldsymbol{u}_t < 0$) to several amps. In the constant current sub-mode, it practically varies from zero during short periods with $\boldsymbol{E}_m \cdot \boldsymbol{u}_t < 0$ to the target value, where it spends most of the time. A detailed inspection of panels (b), (d), and (f) provides more useful information. For instance, just after the beginning of the tenth day, the current goes to zero because $\boldsymbol{E}_m \cdot \boldsymbol{u}_t < 0$ and the code sets $W_e = RI_C^2 = 0$. Afterwards, it is observed that the target current is reached with $R = 0$ and W_e varying below the maximum W_e^{max}. There are phases in panel (b) where I_C is below I_C^* because W_e in panel (d) reaches the maximum available power W_e^{max}.

There are also other phases where $I_C = I_C^*$ with $W_e = 0$. This corresponds to intervals in panel (f) where the resistor is active and it acts as a current limiter. One concludes that the injection of power, even if small, can be beneficial to reach a constant (or almost constant) current at the AEE.

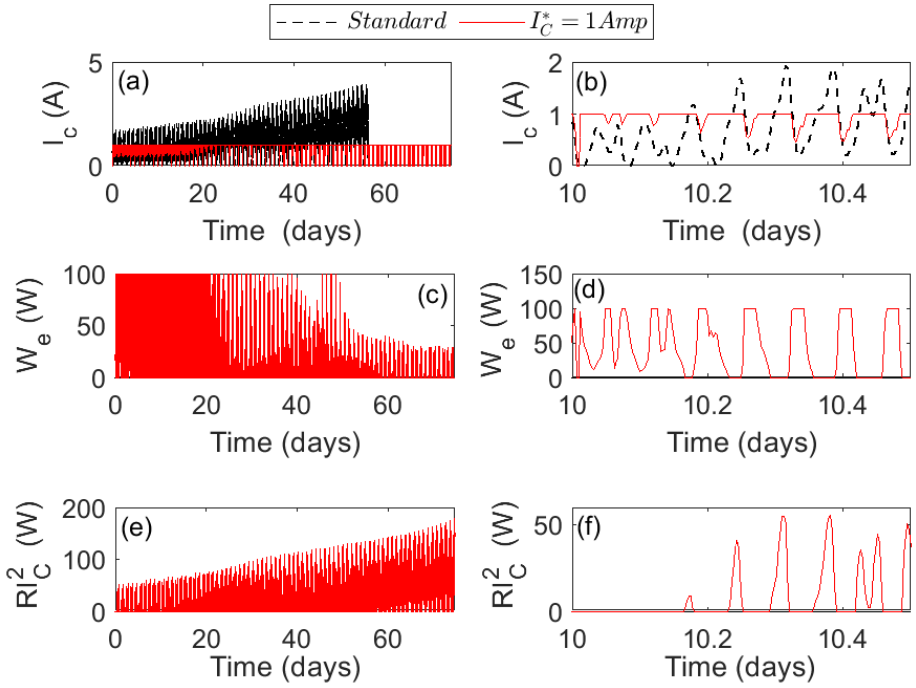

Figure 5: Evolution of the current (top), the power (middle), and the power dissipated in the resistor (bottom), in the standard and the constant current modes for $inc = 60°$.

3.2. *EDT in active mode*

3.2.1. *The Constant Power Submode*

The performances of EDTs in reboost scenarios were studied by considering the parameters of Table 3, and initial and final orbits with altitudes 450 km and $H_F = 600$ km, respectively. The total length of the active segment is $L_a = L_i + L_b = 2$ km. A deep parametric analysis varying the inclination of the initial orbit, the power, and the insulated-to-active tether length ratio $f_i = L_i/L_a$ was carried out (find a summary of the results in Fig. 6). Panels (a),(c) and (e) show the required reboost time versus the orbit inclination for different values of the power and $f_i = 0.5$, 0.65 and 0.8, respectively. For clarity, panels (b), (d), and (f) show the same information but with a different upper limit in the vertical axis.

The reboost time is well below one month for low and middle inclinations. For instance, for 60° of inclination, $f_i = 0.65$ and $W_e = 400$, 700 and 1000 W, the reboost time is around 22, 15, and 12 days, respectively. The parametric analysis also highlights the importance of making a correct design of the tether to reach high performances. For instance, if we focus on the case with 90° of inclination and 400 W of power, we observe that the reboost time is 307, 174, and 214 days for $f_i = 0.5$, 0.65, and 0.8. Therefore, the performances are quite sensitive to the length of the insulated segment. This parametric analyses, which requires a low computational cost, can play an interesting role in the design of EDT reboost missions. Since they use precise environmental models, perturbations, etc, they can provide an accuracy that is halfway between the one provided by analytical or semi-analytical studies [3, 46, 49] and detailed dynamic studies [50, 51, 52].

To assess the impact of the solar cycle, the set of simulations with $f_i = 0.65$ and W_e were repeated but using 1/1/1995 as starting date. As compared with the case of deorbiting shown in Sec. 3.1.1, the solar activity has a moderate impact. In fact, the decrease in the aerodynamic drag is beneficial in this case as the force that needs to be overcome for raising the altitude is lower (i.e., a smaller Lorentz force is necessary). For instance, for inclinations up to 65°, the reboost time is a factor 1.25 larger than the one shown in Fig. 6. Such a factor increases with the inclination and reaches a value around 1.5 for 90° and Sun-Synchronous orbit.

3.2.2. The Constant Current Sub-mode

The constant current sub-mode for a tether in the active mode is similar to the one presented in Sec. 3.1.2, but no resistor is needed as the modulation of the power is enough. The software determines and uses at every time step the

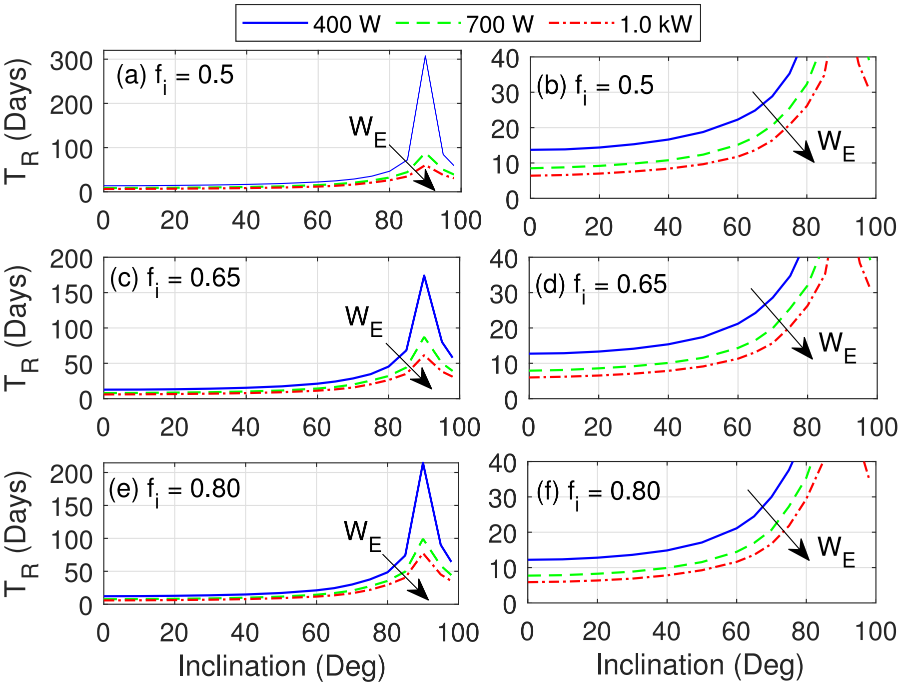

Figure 6: Time for reboosting a 500-kg satellite from a circular orbit of 450 km of altitude to 600 km by using an EDT of dimensions 2 $km \times 2.5\ cm \times 40\ \mu m$. In panels (a)-(c) the fraction of the insulated segment is 0.5, 0.65, and 0.8, respectively.

required power to meet the condition $I_C(t) = I_C^*$, with I_C^* a prescribed value. In case the required power is larger than the maximum available power W_e^{max}, the current and voltage profiles are computed by setting $W_e = W_e^{max}$ and the current at the AEE is lower than I_C^*. To illustrate this sub-mode, we considered the same parameters of Sec. 3.2.1, 60° of inclination and $f_i = 0.65$.

Dashed black lines in panels (a) and (b) of Fig. 7 show the evolution of the current at the AEE in the simulation of Sec. 3.2.1, i.e. with a constant power and equal to $W_e = 400\ W$. It is evident that operating the EDT with a constant power in the reboost mode produces significant variations of the current at the electron emitter. Besides vanishing for $\boldsymbol{E}_m \cdot \boldsymbol{u}_t > 0$, the current varies from around one to two amps, which may not be optimal for the lifetime and the operation of the emitter. Solid red lines in Fig. 7 display the results by using the constant current sub-mode with $I_C^* = 1\ A$ and $W_e^{max} = 500$ W. A power below 400 W is needed to reach 1 Amp at the emitter during most of the maneuver. Nonetheless, there are phases where a power above 500 W is necessary to reach the target current. These phases are identified as the segments where power W_e saturates to 500 W [panel (d)] and the current at the cathode is below 1 Amp [panel (b)]. For this particular set of parameters, moving from the constant power sub-mode to the constant current sub-mode increases the reboost time from 21 to 30 days. In return, the operation of the electron emitter is eased.

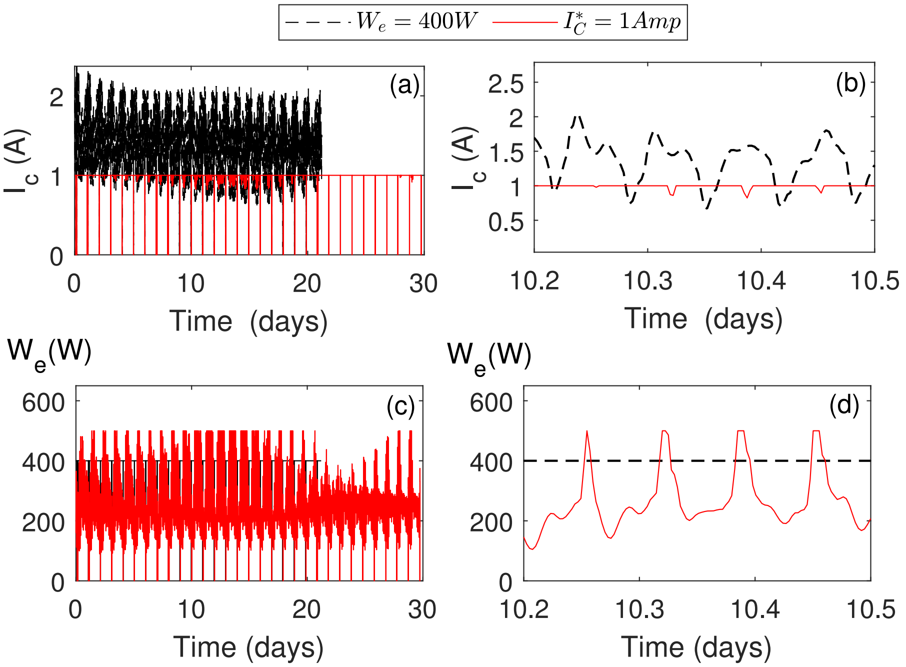

Figure 7: Current at the cathode (top) and injected power (bottom) for the constant power (dashed black lines) and the constant current modes (solid red lines).

4. Conclusions

The electric module, i.e. the algorithm that computes the current and voltage profiles throughout the tether, is a critical component of EDT software because it affects its computational cost and versatility. In the case of BETsMA v2.0, its electric module handles BETs and LWTs in active and passive modes and integrates recent results on Orbital-Motion-Theory (OMT) for emissive probes. As shown in the Appendix, a parametrization proposed in a previous work for BETs in passive mode has been used and extended to cover the two tether types and modes. An important conclusion validated by the simulation campaign of this work is that such strategy yields an efficient and robust code. For instance, 1 day of simulation is typically computed in less than 1 second by a regular workstation. All the simulations of this work, which include parametric analyses of deorbiting and reboost scenarios varying orbit inclination, input power, and tether longitudinal design, are performed in less than 2 hour of machine time. These figures only apply to the tether model assumed in this work, which corresponds to a straight and inelastic tether aligned with the local vertical. The computational cost of the N-bar and N-particle dynamic models for the tether that are available in the software (and were not discussed in this work) is much higher. Regarding versatility, the proposed architecture for the EDT system combines a resistor and a power supply. This allows analyses to cover an interesting range of sub-modes like constant power, constant current, current limited, etc. Besides opening the possibility to study a larger variety of missions, having access to these sub-modes in the simulation tool helps to assess the impact on the performances of additional requirements or constraints. For instance, mitigating the dynamic instability of electrodynamic tethers may require to limit the electric current whereas the operation of the electron emitter and its lifetime can pose boundaries to the maximum and minimum current and its rate of variation. Analysis with the sub-modes of the simulation tool provides key information for the design of the system, like the requirements for the resistor and the power supply.

The simulation analysis revealed that adding a power supply between the bare tether and the electron emitter produces important benefits in deorbiting scenarios. Since the tether operates in the passive mode, such a power supply is not essential, but the performances of the system are enhanced. For instance, it was shown that the required time for deorbiting a 500 kg satellite from a circular orbit of 800 km of altitude and 98° of inclination by a 2 $km \times 2.5\ cm \times 40\ \mu m$ BET decreases from 277 to 158 days by adding 100 W of power. This conclusion is particularly important in post-mission disposal scenarios where the solar panel of the satellites could still provide a significant amount of power. The use of this power by the tether would require a certain level of integration with the satellite but this would be largely compensated by the potential benefits. Aided by this power, and even at high inclinations, a relatively short tether could deorbit satellites within a few months according to the simulation results.

5. Acknowledgements

This work was supported by the European Union's Horizon 2020 Research and Innovation Programme under grant agreement No 828902 (E.T.PACK project). The authors thank ESA Space Debris Office for the useful feedback provided on the interpretation of the data of the space debris flux and the use of MASTER-2009 and MASTER 8

Appendix A. Basic concepts and models

The computation of the average current in Eq. (2) needs the current profile $I(x)$, where x is the tether coordinate measured from point A in Figs. 1 and 2. As usual in EDT modelling [3], we introduce the following dimensionless variables

$$i(\xi) = \frac{I(x)}{|E_m|\sigma_t A_t}, \quad \phi(\xi) = \frac{V(x)}{|E_m| L_*}, \quad \xi = \frac{x}{L_*} \tag{A.1}$$

where $\boldsymbol{I} = I(x)\boldsymbol{u}_t$ is the electric current, $V(x)$ is the tether-to-plasma bias, $E_m \equiv (\boldsymbol{v}_{rel} \times \boldsymbol{B}) \cdot \boldsymbol{u}_t$, σ_t and A_t are the tether conductivity and cross-sectional area and

$$L_* \equiv \left(\frac{2A_t}{p_t}\right)^{2/3} \left(\frac{9\pi^2 m_e \sigma_t^2 |E_m|}{128 e^3 N_0^2}\right)^{1/3}, \tag{A.2}$$

is a characteristic length gauging ohmic effects [3]. In Eq. (A.2), p_t, m_e, e, and N_0 are the tether perimeter, electron mass, elementary charge, and unperturbed plasma density. Subscripts for i, ϕ and ξ denotes their values at a specific point in Figs. 1 and 2. For instance, we will write $i_P = i(\xi_b)$ and $\phi_A = \phi(0)$.

The dimensionless variables are very convenient because the normalized tether-to-plasma bias is then governed by [3]

$$\frac{d\phi}{d\xi} = i(\xi) \mp 1 \tag{A.3}$$

where the upper and lower signs hold for the passive and active modes, respectively. Equation (A.3) is coupled with the normalized electric current $i(\xi)$, which depends on the particular type of tether segment. If bare, the current profile is governed by [3]

$$\frac{di}{d\xi} = \begin{cases} \frac{3}{4}\sqrt{\phi} & \phi > 0 \\ \frac{3}{4}\sqrt{\frac{m_e}{m_i}}\sqrt{-\phi} \approx 0 & \phi < 0 \end{cases} \tag{A.4}$$

where, as usual in bare tether analysis, we assumed Orbital-Motion-Limited (OML) law for high bias ($e|V|/kT_e >> 1$). Current collection beyond the OML regime is incorporated in BETsMA v2 through a re-scaling of the variable L_* as explained in Ref. 31. In the cathodic segment, we used that the electron-to-ion mass ratio is very small ($m_e/m_i << 0$) to write $di/d\xi \approx 0$. For a tether segment coated with a low-W material we use

$$\frac{di}{d\xi} = \begin{cases} -k_c & \phi < \phi^* \\ -k_c\frac{\phi}{\phi^*} & \phi^* < \phi < 0 \\ \frac{3}{4}\sqrt{\phi} & \phi > 0 \end{cases} \tag{A.5}$$

where

$$k_c = \frac{p_t L_*(J_{RD} + J_{ph})}{\sigma_t A_t |E_m|} \tag{A.6}$$

and J_{RD} and J_{ph} the current densities due to the thermionic and the photoelectric effects (find formulas in Ref. 40). Equation (A.5) considers OML current collection (bottom), and SCL (middle) and non-SCL (top) electron emission. As recently shown by detailed kinetic analysis of emissive probes with cylindrical geometry in the framework of the Orbital Motion Theory [47], the transition bias ϕ^* that separates SCL from non-SCL regimes depends on the tether radius-to-Debye length ratio ($\rho = R_t/\lambda_{De}$), the tether-to-electron temperature ratio

$(\delta_t = T_t/T_e)$, the ion-to-electron temperature ration $(\delta_i = T_i/T_e)$ and the emission level

$$\beta(\delta_t) = \left(\frac{2\pi m_e k_B T_e}{h_p^2 N_0^{2/3}} \times \delta_t\right)^{3/2} \exp\left(-\frac{W_t}{k_B T_e} \times \frac{1}{\delta_t}\right) \tag{A.7}$$

with h_p the Planck constant, W_p the work function of the coating, and we assumed that the probe emits electrons following the Richardson-Dushman law. For typical LEO and LWT operational conditions, ϕ^* can be approximated by the minimum between zero and the law [47]

$$\phi^* = \frac{k_B T_e}{e \mid E_m \mid L_*} \times \phi_{p1} \beta^{k_0 + k_1 \left[1 - \left(1 - a\frac{\beta}{\beta_1}\right)\exp\left(-\frac{\beta}{\beta_1}\right)\right]} \tag{A.8}$$

with

$$\phi_{p1} = 0.05\rho - 0.67\sqrt{\rho} + 0.13, \tag{A.9}$$

$$\beta_1 = 44\rho^{-0.9}, \tag{A.10}$$

$$k_0 = 0.94, \tag{A.11}$$

$$k_1 = -0.016\rho + 0.313\sqrt{\rho} - 0.017 \tag{A.12}$$

$$a = \frac{1}{2}\left[1 + \tanh(\rho - 1)\right] \tag{A.13}$$

Since our work considers tape-like tether, we will use Eq. (A.8) with the equivalent radius $R_{eq} = w_t/4$, which was shown to be appropriate for probe analysis at high bias $(e|V|/kT_e >> 1)$ [53].

Regarding the insulated segment, the current is constant $(i_P = i_S)$ and the integration of Eq. (A.3) gives

$$\phi_{S_i} = \phi_P + (i_P \mp 1)\,\xi_i \tag{A.14}$$

with $\xi_i = L_i/L_*$.

The normalized bias difference between points C and S_i at the top panel of Fig. 1 is

$$\phi_C - \phi_{S_i} \equiv f_i(i_C) = \begin{cases} 0 & i = 1 \\ r i_C, & i = 2 \\ -\frac{w_e}{i_C} & i = 3 \end{cases} \tag{A.15}$$

where i_C is the dimensionless current at the AEE. Therefore, the electric model for a BET depends on the normalized lengths

$$\xi_b \equiv \frac{L_b}{L_*}, \qquad \xi_i \equiv \frac{L_i}{L_*} \tag{A.16}$$

and the dimensionless parameters

$$r \equiv \frac{A_t \sigma_t R}{L_*}, \qquad w_e \equiv \frac{W_e}{\sigma_t E_m^2 A_t L_*}, \qquad \phi_C \equiv \frac{V_c}{|E_m| L_*} < 0, \tag{A.17}$$

which correspond to the normalized resistance, input power and potential drop at the AEE, respectively.

For a BET, the current profile is given by the solution of Eq. (A.3) and (A.4) together with (A.15), the equations for the insulated segment, and the boundary conditions

$$i(0) = 0, \quad \phi(\xi_b + \xi_i) = \phi_C \tag{A.18}$$

For a LWT, Eq. (A.4) should be substituted by Eq. (A.5) and the boundary conditions are

$$i(0) = 0, \quad i(\xi_b + \xi_i + \xi_c) = 0 \tag{A.19}$$

However, as shown in Ref. [31] for BETs in passive mode and later for other tether types and modes [40, 10], solving a boundary value problem can be avoided by using an appropriate change of variable and finding (analytical) series expansion of the two functions

$$F_s(z) \equiv \int_0^z \sinh^{1/3} \zeta d\zeta \tag{A.20}$$

$$F_c(z) \equiv \int_0^z \cosh^{1/3} \zeta d\zeta, \tag{A.21}$$

which appears naturally in the analysis of the bare segment. Appendix B and Appendix C give more details about the algorithms.

Appendix B. Passive mode

Appendix B.1. BET

The use of Eqs. (A.3) (with the minus sign) and (A.15) in Eq. (2) gives

$$i_{av} \equiv \frac{I_{av}}{|E_m| \sigma_t A_t} = \frac{1}{\xi_a} \int_0^{\xi_a} i(\xi) d\xi = 1 - \frac{\phi_A - \phi_S}{\xi_a} = 1 - \frac{\phi_A + f_i(i_P) - \phi_C}{\xi_a} \tag{B.1}$$

with $\xi_a = (L_b + L_i)/L_* \equiv \xi_b + \xi_i$ and $i_P = i_S = i_C$. Therefore, the computation of i_{av} does not require the detail of the full current profile but just the two local variables ϕ_A and i_P. They are found from the circuit equation

$$g^P_{BET}(i_P) \equiv \phi_C - f_i(i_P) - (i_P - 1)\xi_i - \phi_P(i_P) = 0 \tag{B.2}$$

and the analysis of the bare segment (see below), which gives the relation $\phi_P(i_P)$.

As shown in Ref. [10], the integration of Eqs. (A.3) (with the minus sign) and upper (A.4) with the boundary conditions $i(0) = 0$ and $\phi(0) = \phi_A$ depends on ϕ_A. For $\phi_A = 1$, one finds

$$\phi(\xi) = \left(1 - \frac{\xi}{4}\right)^4 \tag{B.3}$$

$$i(\xi) = 1 - \left(1 - \frac{\xi}{4}\right)^3 \tag{B.4}$$

This solution is only valid for $\xi < 4$. In case $\xi_b \equiv L_b/L_* > 4$, then we have $\phi = 0$ and $i = 1$ in the segment $4 \le \xi \le \xi_b$. For $\phi_A < 1$, the profiles are

$$\phi(v) = \left(1 - \phi_A^{3/2}\right)^{2/3} \sinh^{4/3} v \tag{B.5}$$

$$i(v) = 1 - \sqrt{1 - \phi_A^{3/2}} \cosh v \tag{B.6}$$

$$\xi(v) = \frac{4}{3}\left(1 - \phi_A^{3/2}\right)^{1/6} \left[F_s(v_{c0}) - F_s(v)\right] \tag{B.7}$$

where we defined the variable $\cosh v_{c0} \equiv 1/\sqrt{1 - \phi_A^{3/2}}$. If $\xi_b < \xi_{AB}$ with

$$\xi_{AB} \equiv \frac{4}{3}(1 - \phi_A^{3/2})^{1/6} F_s(v_{c0}), \tag{B.8}$$

then no cathodic segment develops. Otherwise, Eqs. (B.5)-(B.7) are only valid from $0 \le \xi \le \xi_{AB}$ and, from $\xi_{AB} \le \xi \le \xi_b$ we have

$$i(\xi) = i_P \tag{B.9}$$

$$\phi(\xi) = (i_P - 1)(\xi - \xi_{AB}), \tag{B.10}$$

which are obtained from Eq. (A.3) and bottom (A.4) with the boundary conditions $i(\xi_{AB} = i_P)$ and $\phi(\xi_{AB}) = 0$. For $\phi_A > 1$, one finds

$$\phi(v) = \left(\phi_A^{3/2} - 1\right)^{2/3} \cosh^{4/3} v \tag{B.11}$$

$$i(v) = 1 + \sqrt{\phi_A^{3/2} - 1}\sinh v \tag{B.12}$$

$$\xi(v) = \frac{4}{3}\left(\phi_A^{3/2} - 1\right)^{1/6} \left[F_c(v) - F_c(v_{s0})\right] \tag{B.13}$$

with $\sinh v_{s0} \equiv -1/\sqrt{\phi_A^{3/2} - 1}$. This regime only happens for high enough w_e and no cathodic segment develops.

Variables ϕ_A and i_P in Eq. (B.1) are found by applying a Newton-Raphson method to Eq. (B.2) with ϕ_A as the unknown. Given a value of ϕ_A, function g_{BET}^P is evaluated as follows. If $\phi_A > 1$, then we first compute v_b by solving $\xi(v_b) = \xi_b$ from Eq. (B.13) and, once v_b is known, ϕ_P and i_P are obtained by evaluating Eqs. (B.11)-(B.12) with $v = v_b$. If $\phi_A < 1$, we first compute ξ_{AB} from Eq. (B.8). For $\xi_b < \xi_{AB}$, we first compute v_b by solving $\xi(v_b) = \xi_b$ from Eq. (B.7) and then ϕ_P and i_P from Eqs. (B.5)-(B.6) at $v = v_b$. Otherwise, it is necessary to compute v_{AB} by solving $\xi(v_{AB}) = \xi_{AB}$ with Eq. (B.7), and then i_P evaluating Eq. (B.6) at $v = v_{AB}$ and ϕ_P with Eq. (B.10) evaluated at $\xi = \xi_b$.

Appendix B.2. LWT

For a LWT with a coated segment of length L_c, the normalized average current in passive mode is

$$i_{av} = \frac{1}{\xi_c}\int_0^{\xi_c} i d\xi = \frac{1}{\xi_c}\int_0^{\xi_c}(1 + \frac{d\phi}{d\xi})d\xi = 1 - \frac{\phi_A - \phi_C}{\xi_c} \tag{B.14}$$

where $\xi_c = L_c/L_*$ and variables ϕ_A and ϕ_C are obtained by doing a detailed analysis of the current and voltage profiles. Regarding the anodic segment ($\phi > 0$), they are given by Eqs. (B.6)-(B.7) because for a LWT in passive mode (and without any power supply) we always have $\phi_A < 1$. These laws are valid within the range $0 \le \xi \le \xi_{AB}$, where ξ_{AB} is given by Eq. (B.8).

Regarding the cathodic segment, variables k_t and ϕ^* are evaluated by using a mean tether temperature $T_t = (T_A + T_B)/2$, where T_A and T_B are the minimum and maximum temperatures. They are reached at the anodic point (A) and the zero-bias point (B) because the Joule heating is zero and maximum at these two points. Such a property couples the electric and thermal model in the software. The current and voltage profiles are then found by following Ref. 43 closely. For the range $\xi_{B^*} \leq \xi \leq \xi_C$, the integration of Eq. (A.3) with the minus sign and top Eq. (A.5) with the boundary conditions $i(\xi_C) = 0$ and $\phi(\xi_{B^*}) = \phi^*$ gives

$$\begin{aligned} \phi(\xi) =& \phi^* + \frac{k_c}{2}\left[(\xi_c - \xi_{B^*})^2 - (\xi_c - \xi)^2\right] - (\xi - \xi_{B^*}) && \text{(B.15)} \\ i(\xi) =& k_c\left(\xi_c - \xi\right) && \text{(B.16)} \end{aligned}$$

For the tether range $\xi_{AB} \leq \xi \leq \xi_{B^*}$, we integrate Eq. (A.3) and middle Eq. (A.5) with the boundary conditions $\phi(\xi_{AB}) = 0$ and $i(\xi_{AB}) = i_B = 1 - \sqrt{1 - \phi_A^{3/2}}$ to find

$$\begin{aligned} i(\xi) =& 1 - \sqrt{1 - \phi_A^{3/2}} \cosh\left[\sqrt{\frac{k_c}{|\phi^*|}}\left(\xi - \xi_{AB}\right)\right] && \text{(B.17)} \\ \phi(\xi) =& -\sqrt{\frac{|\phi^*|(1 - \phi_A^{3/2})}{k_c}} \sinh\left[\sqrt{\frac{k_c}{|\phi^*|}}\left(\xi - \xi_{AB}\right)\right], && \text{(B.18)} \end{aligned}$$

The coordinate of the SCL/non-SCL transition point is found by imposing bias continuity at ξ_{B*}

$$\xi_{B^*}(\phi_A) = \xi_{AB} + \sqrt{\frac{|\phi^*|}{k_c}} \sinh^{-1}\left(\sqrt{\frac{\mid \phi_* \mid k_c}{1 - \phi_A^{3/2}}}\right) \tag{B.19}$$

The bias at the anodic point, ϕ_A, is found by solving the nonlinear algebraic equation $g^P_{LWT}(\phi_A) = 0$ with

$$g^P_{LWT} \equiv \begin{cases} k_c\left[\xi_c - \xi_{B^*}\right] - 1 + \sqrt{1 - \phi_A^{3/2}} \cosh\left[\sqrt{\frac{k_c}{|\phi^*|}}\left(\xi_{B^*} - \xi_{AB}\right)\right] & \xi_{B^*} < \xi_c \\ -1 + \sqrt{1 - \phi_A^{3/2}} \cosh\left[\sqrt{\frac{k_c}{|\phi^*|}}\left(\xi_c - \xi_{AB}\right)\right] & \xi_{B^*} > \xi_c \end{cases} \tag{B.20}$$

where $\xi_{AB}(\phi_A)$ and $\xi_{B^*}(\phi_A)$ are given by Eqs. (B.8) and (B.19).

Appendix C. Current and voltage profiles in active mode

Appendix C.1. BET

BETsMA v2 computes the normalized average current for BETs in the active mode by following previous works [3, 46] but with two modifications. First, a non-ideal active electron emitter ($V_C \neq 0$) is consider. Second, in order to speed-up the code, BETsMA does not leave certain lengths in integral form [see for instance Eqs. (16a) and (16b) in Ref. 46], but takes advantage of the analytical series of function F_s and F_c. For instance, the anodic length is given by [40]

$$\frac{L_{anodic}}{L_*}\left(\phi_A, i_B\right) = \begin{cases} \frac{4}{3}\left(1-\phi_A^{3/2}\right)^{1/6}\left[F_s\left(v_{cf}\right)-F_s\left(v_{c0}\right)\right], & \phi_A < 1, \\ 4\left[\left(1+i_B\right)^{1/3}-1\right], & \phi_A = 1 \\ \frac{4}{3}\left(\phi_A^{3/2}-1\right)^{1/6}\left[F_c\left(v_{sf}\right)-F_s\left(v_{s0}\right)\right], & \phi_A > 1, \end{cases} \quad , \tag{C.1}$$

which is obtained from Eq. (A.3) (with the positive sign) and upper Eq. (A.4) with $i(0) = 0$ and $\phi(L_{anodic}/L_*) = 0$. Here $\cosh\left(v_{cf}\right) = \left(1+i_B\right)/\sqrt{1-\phi_A^{3/2}}$, $\cosh\left(v_{c0}\right) = 1/\sqrt{1-\phi_A^{3/2}}$, $\sinh\left(v_{sf}\right) = \left(1+i_B\right)/\sqrt{\phi_A^{3/2}-1}$, $\sinh\left(v_{s0}\right) = 1/\sqrt{\phi_A^{3/2}-1}$.

Appendix C.2. LWT

The electric model of BETsMA v2.0 for LWTs in the active mode is presented in Ref. [40], except that now the SCL transition point is given by Eq. A.8.

References

[1] D. Baiocchi, W. Welser, The Democratization of Space New Actors Need New Rules, FOREIGN AFFAIRS 94 (3) (2015) 98–104.

[2] J. R. Sanmartin, E. C. Lorenzini, Martinez-Sanchez, Electrodynamic Tether Applications and Constraints, Journal of Spacecraft and Rockets 47 (2010) 442–456. `doi:10.2514/1.45352`.

[3] J. R. Sanmartin, M. Martinez-Sanchez, E. Ahedo, Bare wire anodes for electrodynamic tethers, Journal of Propulsion Power 9 (1993) 353–360. `doi:10.2514/3.23629`.

[4] S. B. Khan, J. R. Sanmartin, Survival probability of round and tape tethers against debris impact, Journal of Spacecraft and Rockets 50 (2013) 603–608. `doi:10.2514/1.A32383`.

[5] A. Francesconi, C. Giacomuzzo, L. Bettiol, E. Lorenzini, A new ballistic limit equation for thin tape tethers, Acta Astronautica 129 (2016) 325 – 334. `doi:https://doi.org/10.1016/j.actaastro.2016.09.023`.
URL `http://www.sciencedirect.com/science/article/pii/S0094576516303988`

[6] K. Makihara, S. Kondo, Structural evaluation for electrodynamic tape tethers against hypervelocity space debris impacts, Journal of Spacecraft and Rockets 55 (2) (2018) 462–472. `arXiv:https://doi.org/10.2514/1.A34023`, `doi:10.2514/1.A34023`.
URL `https://doi.org/10.2514/1.A34023`

[7] J. D. Williams, J. R. Sanmartín, L. P. Rand, Low work-function coating for an entirely propellantless bare electrodynamic tether, IEEE Transactions on Plasma Science 40 (2012) 1441–1445. `doi:10.1109/TPS.2012.2189589`.

[8] G. Sanchez-Arriaga, X. Chen, Modeling and performance of electrodynamic low-work-function tethers with photoemission effects, Journal of Propulsion and Power 34 (1) (2018) 213–220. `doi:10.2514/1.B36561`.

[9] C. Huo, F. Liang, A. Sun, Review on development of carbon nanotube field emission cathode for space propulsion systems, High Voltage 5 (4) (2020) 409–415. `doi:10.1049/hve.2019.0257`.

[10] M. Tajmar, G. Sanchez-Arriaga, A bare-photovoltaic tether for consumable-less and autonomous space propulsion and power generation, Acta Astronautica.

[11] T. Sato, S. Kawamoto, Y. Ohkawa, T. Watanabe, K. Kamachi, H. Okubo, Performance of edt system for deorbit devices using new materials, Acta Astronautica 177 (2020) 813 – 820. `doi:https://doi.org/10.1016/j.actaastro.2020.01.029`.
URL `http://www.sciencedirect.com/science/article/pii/S0094576520300400`

[12] I. C. Bell, B. E. Gilchrist, J. K. McTernan, S. G. Bilén, Investigating miniaturized electrodynamic tethers for picosatellites and femtosatellites, Journal of Spacecraft and Rockets 54 (1) (2017) 55–66. `doi:10.2514/1.A33629`.

[13] Z. Zhu, Mission design of deorbiting spacecraft using electrodynamic tethers (DESCENT), The International Conference on Aerospace System Science and Engineering, ICASSE 2017, Shanghai, China, 2017.

[14] G. Sánchez-Arriaga, S. Naghdi, K. Wätzig, J. Schilm, E. Lorenzini, M. Tajmar, E. Urgoiti, L. T. Castellani, J. Plaza, A. Post, The E.T.PACK project: Towards a fully passive and consumable-less deorbit kit based on low-work-function tether technology, Acta Astronautica 177 (2020) 821–827. `doi:10.1016/j.actaastro.2020.03.036`.
URL `https://doi.org/10.1016/j.actaastro.2020.03.036`

[15] S. Garcia-Gonzalez, G. Sánchez-Arriaga, Attitude determination and control for the deployment preparation phase of a space tether mission, Submited to Acta Astronautica.

[16] S. Bilen, J. McTernan, B. Gilchrist, I. Bell, N. Voronka, R. Hoyt, Electrodynamic tethers for energy harvesting and propulsion on space platforms, in: AIAA SPACE 2010 Conference & Exposition, American Institute of Aeronautics and Astronautics, 2010. `doi:10.2514/6.2010-8844`.
URL `https://doi.org/10.2514/6.2010-8844`

[17] R. Mantellato, L. Olivieri, E. Lorenzini, Study of dynamical stability of tethered systems during space tug maneuvers, Acta Astronautica 138

(2017) 559–569. `doi:10.1016/j.actaastro.2016.12.011`.
URL `https://doi.org/10.1016/j.actaastro.2016.12.011`

[18] G. Li, Z. H. Zhu, Multiphysics finite element modeling of current generation of bare flexible electrodynamic tether, Journal of Propulsion and Power 33 (2) (2017) 408–419. `arXiv:https://doi.org/10.2514/1.B36211`, `doi:10.2514/1.B36211`.
URL `https://doi.org/10.2514/1.B36211`

[19] R. Hoyt, Design and simulation of a tether boost facility for leo to gto transport, in: 36th AIAA/ASME/SAE/ASEE Joint Propulsion Conference and Exhibit, 2000. `arXiv:https://arc.aiaa.org/doi/pdf/10.2514/6.2000-3866`, `doi:10.2514/6.2000-3866`.
URL `https://arc.aiaa.org/doi/abs/10.2514/6.2000-3866`

[20] G. Sánchez-Arriaga, C. Bombardelli, X. Chen, Impact of nonideal effects on bare electrodynamic tether performance, Journal of Propulsion and Power 31 (3) (2015) 951–955. `doi:10.2514/1.B35393`.

[21] J. Pelaez, E. C. Lorenzini, O. Lopez-Rebollal, M. Ruiz, A new kind of dynamic instability in electrodynamic tethers, in: Advances in the Astronautical Sciences, Vol. 105, pp. 1367-1386, Spaceflight Mechanics, AAS Publications, San Diego, CA, 2000., p.1367, Vol. 105, 2000, pp. 1367–1386.

[22] E. L. M. Lanoix, A. K. Misra, V. J. Modi, G. Tyc, Effect of electromagnetic forces on the orbital dynamics of tethered satellites, Journal of Guidance, Control, and Dynamics 28 (6) (2005) 1309–1315. `arXiv:https://doi.org/10.2514/1.1759`, `doi:10.2514/1.1759`.
URL `https://doi.org/10.2514/1.1759`

[23] E. M. Levin, J. Pearson, J. C. Oldson, Dynamics simulation model for space tethers, NASA/CR—2006–214432 Available from NASA Center for AeroSpace Information (2006) 1–70. `doi:10.1016/S0045-7825(01)00163-3`.

[24] K. Kristiansen, P. Palmer, R. Roberts, Numerical modelling of elastic space tethers, Celestial Mechanics and Dynamical Astronomy 113. `doi:10.1007/s10569-012-9411-5`.

[25] R. Zhong, Z. H. Zhu, Dynamics of nanosatellite deorbit by bare electrodynamic tether in low earth orbit, Journal of Spacecraft and Rockets 50 (3) (2013) 691–700. `arXiv:https://doi.org/10.2514/1.A32336`, `doi:10.2514/1.A32336`.
URL `https://doi.org/10.2514/1.A32336`

[26] C. Bombardelli, D. Zanutto, E. Lorenzini, Deorbiting performance of bare electrodynamic tethers in inclined orbits, Journal of Guidance, Control, and Dynamics 36 (5) (2013) 1550–1556. `doi:10.2514/1.58428`.
URL `https://doi.org/10.2514/1.58428`

[27] S. Kawamoto, Y. Ohkawa, T. Okumura, K. Iki, H. Okamoto, Performance of electrodynamic tether system for debris deorbiting: Re-evaluation based on the results of kite experiments, in: 69th International Astronautical Congress (IAC), Bremen, Germany, Vol. IAC-18- A6.6.5, 2018, p. 1–5.

[28] H. Wen, D. Jin, H. Hu, Three-dimensional deployment of electro-dynamic tether via tension and current control with constraints, Acta Astronautica 129 (2016) 253 – 259. `doi:https://doi.org/10.1016/j.actaastro.2016.09.019`.
URL `http://www.sciencedirect.com/science/article/pii/S0094576516306099`

[29] M. Leamy, A. Noor, T. Wasfy, Sensitivity analysis of bare-wire space tether systems, Computer Methods in Applied Mechanics and Engineering 190 (2001) 5495–5503. `doi:10.1016/S0045-7825(01)00163-3`.

[30] C. Bombardelli, J. Pelaez, M. Sanjurjo, Asymptotic solution for the current profile of passive bare electrodynamic tethers, Journal of Propulsion and Power 26 (6) (2010) 1291–1304. `doi:10.2514/1.46808`.

[31] M. Sanjurjo-Rivo, G. Sánchez-Arriaga, J. Peláez, Efficient computation of current collection in bare electrodynamic tethers in and beyond oml regime, Journal of Aerospace Engineering 28 (6) (2015) 04014144. doi:10.1061/(ASCE)AS.1943-5525.0000479.

[32] J. Pearson, E. Levin, J. Oldson, J. Carroll, ElectroDynamic Debris Eliminator (EDDE): Design, Operation, and Ground Support, in: S. Ryan (Ed.), Advanced Maui Optical and Space Surveillance Technologies Conference, 2010, p. E61.

[33] G. Borderes-Mota, G. Sánchez-Arriaga, Online version of betsma v2.0, https://betsma.uc3m.es, accessed: 2020-12-31.

[34] J. R. Sanmartin, A. Sanchez-Torras, S. B. Khan, G. Sanchez-Arriaga, M. Charro, Optimum Sizing of Bare-Tape Tethers for De-Orbiting Satellites at end of Mission, Advances in Space Research 56 (2015) 1485–1492.

[35] Sánchez-Arriaga, BETsMA Manual, https://www.thebetsproject.com/resources (2014) 1–44.

[36] and C. C. Finlay, S. Maus, C. D. Beggan, T. N. Bondar, A. Chambodut, T. A. Chernova, A. Chulliat, V. P. Golovkov, B. Hamilton, M. Hamoudi, R. Holme, G. Hulot, W. Kuang, B. Langlais, V. Lesur, F. J. Lowes, H. Lühr, S. Macmillan, M. Mandea, S. McLean, C. Manoj, M. Menvielle, I. Michaelis, N. Olsen, J. Rauberg, M. Rother, T. J. Sabaka, A. Tangborn, L. Tøffner-Clausen, E. Thébault, A. W. P. Thomson, I. Wardinski, Z. Wei, T. I. Zvereva, International geomagnetic reference field: the eleventh generation, Geophysical Journal International 183 (3) (2010) 1216–1230. doi:10.1111/j.1365-246x.2010.04804.x.
URL https://doi.org/10.1111/j.1365-246x.2010.04804.x

[37] D. Bilitza, D. Altadill, Y. Zhang, C. Mertens, V. Truhlik, P. Richards, L.-A. McKinnell, B. Reinisch, The international reference ionosphere 2012 – a model of international collaboration, Journal of Space Weather and Space

Climate 4 (2014) A07. `doi:10.1051/swsc/2014004`.
URL `https://doi.org/10.1051/swsc/2014004`

[38] D. Rees, CIRA - Status and the Development of New Reference Models, in: 39th COSPAR Scientific Assembly, Vol. 39, 2012, p. 1600.

[39] J. M. Picone, A. E. Hedin, D. P. Drob, A. C. Aikin, NRLMSISE-00 empirical model of the atmosphere: Statistical comparisons and scientific issues, Journal of Geophysical Research: Space Physics 107 (A12) (2002) SIA 15–1–SIA 15–16. `doi:10.1029/2002ja009430`.
URL `https://doi.org/10.1029/2002ja009430`

[40] G. Sánchez-Arriaga, J. Sanmartín, Electrical model and optimal design scheme for low work-function tethers in thrust mode, Aerospace Science and Technology 96 (2020) 105519. `doi:https://doi.org/10.1016/j.ast.2019.105519`.

[41] G. de Haro Pizarroso, G. Sanchez-Arriaga, A robust multi-body dynamical model for the dynamic simulation of electrodynamic tethers - (-) ((in preparation)) –. `doi:-`.

[42] R. D. Estes, J. R. Sanmartín, Cylindrical Langmuir probes beyond the orbital-motion-limited regime, Physics of Plasmas 7 (2000) 4320–4325. `doi:10.1063/1.1288400`.

[43] X. Chen, J. R. Sanmartín, Bare-tether cathodic contact through thermionic emission by low-work-function materials, Physics of Plasmas 19 (7) (2012) 073508. `arXiv:https://doi.org/10.1063/1.4736987`, `doi:10.1063/1.4736987`.
URL `https://doi.org/10.1063/1.4736987`

[44] J. Peláez, J. M. Hedo, P. R. de Andrés, A special perturbation method in orbital dynamics, Celestial Mechanics and Dynamical Astronomy 97 (2) (2007) 131–150. `doi:10.1007/s10569-006-9056-3`.
URL `https://doi.org/10.1007/s10569-006-9056-3`

[45] E. Ahedo, J. R. Sanmartin, Analysis of bare-tether systems for deorbiting low-earth-orbit satellites, Journal of Spacecraft and Rockets 39 (2) (2002) 198–205. `doi:10.2514/2.3820`.

[46] J. R. Sanmartin, R. D. Estes, E. C. Lorenzini, S. A. Elaskar, Efficiency of electrodynamic tether thrusters, Journal of Spacecraft and Rockets 43 (3) (2006) 659–666. `arXiv:https://doi.org/10.2514/1.16174`, `doi:10.2514/1.16174`.
URL `https://doi.org/10.2514/1.16174`

[47] S. Sadaf, C. Xin, S.-A. G., Parametrization of current-voltage characteristics and operation domains of cylindrical emissive probes in collisionless maxwellian plasmas at rest, Plasma Physics and Controlled Fusion.

[48] J. Sanmartin, M. Charro, E. Lorenzini, H. Garrett, C. Bombardelli, C. Bramanti, Electrodynamic tether at jupiter—i: Capture operation and constraints, IEEE Transactions on Plasma Science 36 (5) (2008) 2450–2458. `doi:10.1109/TPS.2008.2002580`.

[49] G. Khazanov, E. Krivorutsky, D. Gallagher, Electrodynamic bare tether systems as a thruster for the momentum-exchange/electrodynamic reboost (mxer) project, Journal of Geophysical Research 111. `doi:10.1029/2005JA011205`.

[50] H. Lu, Y. Zabolotnov, A. Li, Impact analysis and orbit reboost of payload tossing using spinning electrodynamic tether system, INTERNATIONAL JOURNAL OF ENGINEERING SYSTEMS MODELLING AND SIMULATION 11 (4, SI) (2020) 176–185. `doi:{10.1504/IJESMS.2020.111264}`.

[51] J. Liu, L. Gangqiang, Z. H. Zhu, X. Zhan, Orbital boost characteristics of spacecraft by electrodynamic tethers with consideration of electric-magnetic-dynamic energy coupling, Acta Astronautica 171. `doi:10.1016/j.actaastro.2020.03.001`.

[52] Y. Li, A. Li, C. Wang, H. Tian, Dynamic Analysis and Libration Control of Electrodynamic Tether for Reboost Applications, IEEE ACCESS 9 (2021) 77894–77904. `doi:{10.1109/ACCESS.2021.3083067}`.

[53] J. R. Sanmartin, R. D. Estes, The orbital-motion-limited regime of cylindrical langmuir probes, Physics of Plasmas 6 (1) (1999) 395–405. `doi:10.1063/1.873293`.
URL `https://doi.org/10.1063/1.873293`